Solid-like and liquid-like granular flows on inclined surfaces under vibration – Implications for earthquake-induced landslides

Solid-like and liquid-like granular flows on inclined surfaces under vibration – implications for earthquake-induced landslides

Chongqiang Zhu[a,b], Yu Huang[a], Jin Sun[a,b]*

[a] Department of Geotechnical Engineering, College of Civil Engineering, Tongji University, Shanghai 200092, China

[b] School of Engineering, University of Edinburgh, Edinburgh EH9 3JL, U.K.

* Corresponding author. Tel: +44-131-6519028. E-mail: j.sun@ed.ac.uk

Abstract

Earthquake-induced landslides can result in serious property damage and significant casualties. Although extensive research has been conducted to investigate their extraordinarily long runout, the underlying mechanism remains a very challenging open problem. In this paper, we explore the effect of vibration on landslide runout through simulations of simplified granular chute flows using the discrete element method with a focus on surface-normal vibration. We show that the mobility of the flows is enhanced by low-frequency vibration for inclination angles of both 19° and 24°. The flows are, however, strikingly different – solid-like for the former and liquid-like for the latter, as revealed by their microstructure and stress states. The vibration enhances the mobility through reduction in the normal load and in the solid volume fraction for the 19° and the 24° flows respectively. This work reveals complexities in the rheological states and the dynamic responses of inclined-surface granular flows under vibration, serving as an initial step to unravelling the full dynamic mechanisms of the long runout of earthquake-induced landslides.

Keywords: earthquake-induced landslides; discrete element method (DEM); granular rheology; chute flow; enhanced mobility.

Nomenclature

List of Acronyms

MAM	Multiplex Acceleration Model
DDA	Discontinuous Deformation Analysis
DEM	Discrete Element Method
LAMMPS	Large-scale Atomic/Molecular Massively Parallel Simulator
BNS	Bulk Normal Stress
VA	Vibration Acceleration
NV	No Vibration
BVF	Bulk Volume Fraction
BNS	Bulk Normal Force

1 Introduction

Earthquake-induced landslides exhibit salient characteristics of large volume, high speed and long runout, and can thus result in serious property damage and significant casualties. The catastrophic Wenchuan earthquake in China induced almost 200,000 landslides, which led to about 20,000 fatalities [1]. The Donghekou landslide, for example, caused 10 million m^3 of geomaterials to fail and rapidly flow as long as 2400 m. The rapid long runout landslide buried seven villages and killed 400 villagers [2]. More recently, the 2016 Kumamoto earthquake in Japan triggered more than 3000 landslides causing serious damage in Kyushu island [3]. In general, massive mountainous regions worldwide are at high risk of earthquake-induced landslides according to the studies of regional landslide susceptibility [4-8]. Hence, it is significant and urgent to investigate the mobility of these earthquake-induced landslides to provide guidelines for prevention and mitigation of these disasters.

The high-speed and long-runout mechanism of earthquake-induced landslides is a cutting-edge research aspect in geotechnical engineering worldwide. In previous studies, many mechanisms have been proposed, such as air-lubrication [2], sliding-surface liquefaction induced by grain crushing [9], fluidization [10], momentum transfer [11-12], etc. However, no consensus has been reached regarding the

mechanism of high-speed and long-runout. The above-mentioned mechanisms focus on the reduction of geomaterial strength without considering the earthquake vibration effects. Some pioneering research has demonstrated that seismic vibration is significant to geomaterial flow dynamics. A series of model tests under sinusoidal waves were conducted to study the effect of frequency and amplitude of vibration on the runout of rock avalanches [13-14], and showed that vibration can greatly enhance the mobility of geomaterial flows. Specifically, the runout of geomaterials increased with the amplitude and decreased with the frequency. However, the mechanism of enhanced mobility due to vibration was not presented. A multiplex acceleration model (MAM) was proposed to describe the energy transfer during flow subjected to vibration by studying one particles movement under sinusoidal vibration in shaking table tests [15]. The extended MAM was then successfully applied to discontinuous deformation analysis (DDA) to simulate runout of real earthquake-induced landslides [16-18]. Although the MAM model can partly explain the enhanced mobility of landslides due to earthquakes and also simulate the flow process of real landslides, it was limited by its assumption of rigid block dynamics under seismic condition. The geomaterials in earthquake-induced landslides are usually composed of numerous granular particles instead of only a rigid block. Moreover, earthquake-induced landslides always start from initial translational slides (i.e. solid-like state) and then evolves into large deformation flow (i.e. liquid-like state) [19-20], where the effect of seismic load is expected to be different in different stages. It is thus important to explore the mechanisms for different states based on granular mechanics.

In this work, we simulate flows of granular materials on an inclined-surface (chute) under various vibrating conditions matching realistic earthquake accelerations by resolving the motion of individual particles. In contrast to the previous simulations of transverse vibration parallel to the surface [21], we focus on vibration normal to the surface. We also study the effects of vibration to an initially static granular bed and a fully developed flow respectively at 19° and 24° two inclination angles, reflecting the dynamics at the stages of translational slides and large deformation in an earthquake-

induced landslide. Through analysis of the macroscopic velocities, stresses, rheology and the microstructure of particle contacts, we show that the flows have solid-like and liquid-like behavior respectively at the two angles and that the mechanisms enhancing the mobility are distinct from each other.

This work studies the first-order effect of vibration on landslides mobility, particularly focusing on contrasting two different flow conditions with the same material. The effects of particle properties, such as their size distribution and shapes, are thus not considered and not expected to change the conclusions of this paper.

The rest of the paper is arranged as follows. Firstly, the numerical methodology and the simulation details of the chute flow model are introduced in Sections 2 and 3, respectively. The simulation results are then presented and interpreted in Section 4. Finally, we draw conclusions based on the analysis in Section 5 and present further remarks in Section 6.

2 Methodology and the numerical scheme

To study both the bulk flow and the particle dynamics in detail, it is advantageous to use the well-developed discrete element method (DEM) [22], which tracks the motion of every particle. DEM simulations have been used widely to study granular flows including inclined-surface flows with [21] and without vibration [23-24]. Nevertheless, this numerical method cannot yet simulate full scale landslides due to the prohibitive computational cost in solving the motion equations for an extremely-large number of particles. We thus employ DEM to study the inclined-surface flow of a representative number of spheres as a simplified system to understand the landslide flow behavior and the mechanisms to the enhanced mobility under vibration. The DEM simulations were conducted using an open-source code LAMMPS (Large-scale Atomic/Molecular Massively Parallel Simulator) [25]. LAMMPS has been extensively used in geotechnical engineering simulating, e.g. compression of crushable sand [26], instability of granular soil induced by water infiltration [27], triaxial compression of geomaterials [28], mechanics of sand-rubber mixtures [29], etc. These studies have shown the suitability of using LAMMPS for geotechnical problems.

In DEM, the Newtonian motion equations of each particle *i*

$$\frac{d\boldsymbol{v_i}}{dt} = \boldsymbol{a_i} = \boldsymbol{g} + \frac{1}{m_i}\sum_j \boldsymbol{F}_{ij}^n + \boldsymbol{F}_{ij}^t \quad , \tag{1}$$

$$\frac{d\omega_i}{dt} = \frac{1}{I_i}\sum_j \boldsymbol{x_{ij}} \times \boldsymbol{F}_{ij}^t \quad , \tag{2}$$

are solved, in which m_i, I_i , $\boldsymbol{x_i}$, $\boldsymbol{v_i}$, $\boldsymbol{\omega_i}$, $\boldsymbol{a_i}$ and $\boldsymbol{g}$ are the mass, moment of inertia, position, velocity, rotational velocity and acceleration of particle *i*, and the gravitational acceleration, respectively. The contact forces between particles *i* and *j* can be modelled using a linear spring-dashpot model. The normal and tangential forces are calculated as

$$\boldsymbol{F}_{ij}^n = k_n \delta_{ij} \boldsymbol{n}_{ij} - \gamma_n m_{eff} \boldsymbol{v}_{ij}^n \quad , \tag{3}$$

$$\boldsymbol{F}_{ij}^t = -k_t \boldsymbol{u}_{ij}^t - \gamma_t m_{eff} \boldsymbol{v}_{ij}^t \quad , \tag{4}$$

in which k, γ, $\boldsymbol{v_{ij}}$ are stiffness, damping constant and relative velocity, respectively; δ_{ij} is particle overlap; $\boldsymbol{n}_{ij}$ represents the unit vector along the line of granular center; m_{eff} is effective mass; and $\boldsymbol{u}_{ij}^t$ is the elastic tangential displacement. Particle friction is implemented when the Coulomb yield criterion is satisfied, i.e. $\left|\boldsymbol{F}_{ij}^t\right| > \mu\left|\boldsymbol{F}_{ij}^n\right|$, where μ is friction coefficient.

The motion equations are explicitly integrated using the second-order velocity-Verlet algorithm as

$$\boldsymbol{v}_i^{n+1/2} = \boldsymbol{v}_i^n + \frac{\Delta t}{2}\boldsymbol{a}_i^n \quad , \tag{5}$$

$$\boldsymbol{x}_i^{n+1} = \boldsymbol{x}_i^n + \Delta t \boldsymbol{v}_i^{n+1/2} \quad , \tag{6}$$

$$\boldsymbol{v}_i^{n+1} = \boldsymbol{v}_i^{n+1/2} + \frac{\Delta t}{2}\boldsymbol{a}_i^{n+1} \quad , \tag{7}$$

where n is the number of time steps and Δt is the time increment. The DEM algorithm is illustrated in the flowchart in Fig. 1.

3 Chute flow simulation and post-processing details

Chute flow was simulated using 10569 monodisperse spherical particles, including 979 boundary particles and 9590 flow particles in the configuration presented in Fig. 2. The

diameter and density of particles are d and ρ, respectively. The base surface dimensions of this model are $20d \times 10d$. The initial height of flow particles is $40d$. The inclination angle of this chute flow model is θ. The direction of gravity $\boldsymbol{g}$ is vertically downward. The particles can flow along x direction. The boundaries in x and y directions are both periodic, which prescribes that if a particle leaves the domain through one periodic boundary, it re-enters the domain through the boundary in the opposite direction as if it continues its trajectory. In this way, the periodic boundary condition realizes flow in an infinite domain using finite particles and eliminates the effects of a solid-wall boundary. The z-direction is fixed at bottom and is open at top. The base of $4d$ thickness consists of randomly close-packed particles of diameter d to form a rough boundary. A sinusoidal vibration of frequency f and displacement amplitude A is input to the system by controlling the displacement of the rough base. we set the acceleration amplitude ($4\pi^2 f^2 A$) to be $0.5g$ according to the findings from detailed field survey, that deep-seated landslides were often triggered by earthquakes with peak ground acceleration about $0.5g$ [30].

The quantities in our simulation are made non-dimensional using the following scaling relationship for distance d_0, time $t_0 = \sqrt{d/g}$, velocity $v_0 = \sqrt{gd}$, force $F_0 = g\rho d^3$, elastic constants $k_0 = g\rho d^2$ and stress $\sigma_0 = g\rho d$ [23]. The non-dimensionalization facilitates similitude and scaling analysis and allows presenting the dynamics of vibration-induced flows transcending different physical systems. We set the particle friction coefficient $\mu = 0.5$, normal elastic constant $k_n = 2\times10^5\ g\rho d^2$, tangential elastic constant $k_t = 2/7\ k_n$, normal viscous damping constant $\gamma_n = 50\ \sqrt{gd}$ and the tangential viscous damping constant $\gamma_t = 1/2\ \gamma_n$ [23-24]. The time step was set to be $10^{-4}\ \sqrt{d/g}$, which is about one-fiftieth of contact time [31]. The mobility of the granular system without vibration at different angles was simulated using above parameters and the angle of repose was determined as 19°, at which the granular bed remains static without vibration. The granular bed can reach steady inertial flow at the inclination angle of 24° without vibration [23]. The chute was thus inclined at 19° and 24° to probe the effects

of vibration, reflecting the initial translational sliding and the large-deformation flowing state in earthquake-induced landslides.

Seismic vibration can be decomposed into surface-normal and surface-parallel vibrations. The effects of surface-parallel vibration at the initial translational sliding state were widely studied using the classic Newmark's method [32-36]. We thus focus on studying granular dynamic behavior under surface-normal vibration.

The simulations ran (more than 6×10^7 steps) to reach a dynamic steady state, where the velocity profile at the same phase angle will not change with time. Post-processing was performed using only the steady-state data. The bulk quantities, such as velocity, volume fraction, stress, etc., are calculated using spatial and time averaging. The stress tensor is determined as

$$\boldsymbol{\sigma} = \frac{1}{V}\sum_i \left[\sum_{j\neq i}\frac{1}{2}\boldsymbol{r}_{ij}F_{ij} + m_i(\boldsymbol{v}_i - \overline{\boldsymbol{v}})(\boldsymbol{v}_i - \overline{\boldsymbol{v}})\right], \quad (8)$$

where V is the sampling volume, $\overline{\boldsymbol{v}}$ is averaged velocity. Pressure is calculated as $P = (\sigma_{xx}+\sigma_{yy}+\sigma_{zz})/3$ and shear stress is $\tau = \sigma_{xz}$. The averaging volume uses bins of thickness $1d$ in z-direction and spanning the x-y plane. The space-averaged quantities were further time-averaged at the same phase angle. In this paper, we present our results at four typical phase angles of 0, T/4, T/2 and 3T/4, where T is the vibration period.

4. Results and interpretation

We firstly discuss the effect of vibration frequency at the inclination angle of 19° and 24°. Then the chute flow mobility under z-direction vibration of frequency $0.1\sqrt{g/d}$ will be discussed in detail.

4.1 Effect of vibration frequency

The frequency of an earthquake is typically around 0.1Hz to 20Hz, although an earthquake with frequency up to 165 Hz was also reported [37]. We conducted simulations at the fixed acceleration of $0.5g$, with a range of frequencies at $0.1\sqrt{g/d}$, $0.2\sqrt{g/d}$, $1\sqrt{g/d}$ and $10\sqrt{g/d}$, which corresponds to 1.4Hz, 2.8Hz, 14Hz and 140Hz respectively in real world units, when the dimension and acceleration ratios are chosen

to be 1:0.05 and 1:9.8 (simulation model : prototype). The *x*-velocity profiles of the 19° case at 1/2T under different *z*-direction vibrations are shown in Fig. 3(a). The granular bed is nearly static under vibration with frequency of $10\sqrt{g/d}$ and begins to flow at lower frequencies of $1\sqrt{g/d}$, $0.2\sqrt{g/d}$ and $0.1\sqrt{g/d}$. The velocity monotonically increases with decreasing frequencies. For the 24° case, vibrations can affect the mobility only when the frequency decreases to $0.2\sqrt{g/d}$ and $0.1\sqrt{g/d}$ in Fig. 3(b). It can thus be concluded that the mobility of the chute flow is enhanced by vibration of low frequencies, calling for attention to low-frequency seismic waves, e.g. the near-source pulse-like seismic waves.

4.2 Initial translational sliding state

The *x*-velocity profiles for the 19° case under vibration of $0.1\sqrt{g/d}$ frequency are shown in Fig.4 (a) at different phase angles. It can be seen that the granular bed becomes unstable and gains velocity under vibration, which means that vibration can effectively reduce the stability of slopes and enhance the mobility at the initial translational sliding state. The velocity at T/2 reaches the maximum, while the minimum velocity is observed at 0 or T. The velocity profiles at T/4 and T/2 are S-shaped, while those at 0 and 3T/4 are approximately downward parabolic. These velocity profiles are distinct from a plug flow with parabolic flow profiles. Volume fraction Φ, defined as the ratio of volume occupied by grains to the sampling volume, represents the denseness of a granular system and is an important state variable for granular dynamics. The volume fraction profiles along the height at different phases angles, Fig.4 (b), do not deviate from that of a static granular bed (the black line), which is roughly constant along height. This indicates that the flow under such vibration exhibits solid-like behavior.

To further understand the solid-like characteristics of the flow, the contact force networks and the stresses in the granular bed were analyzed. The normal contact forces between particles are visualized by bonds connecting particle centers with thickness proportional to the magnitudes of the forces, in Fig.5. The contact forces form networks spanning the whole granular bed at all the vibration phases, having similar structures

but different mean force magnitudes. This further confirms the solid-like microstructure and indicates that the average stress magnitude should change with vibration and the shear to normal stress ratio should remain largely unchanged, which has been shown to be determined by the microstructure anisotropy [38].

Indeed, the stresses, Fig.6 (a) and (b), can be seen to vary in magnitude with the vibration and the largest and smallest ones correspond to the strongest and weakest force networks in Fig.5 (d) and (b) at 3/4 T and 1/2 T, respectively. The stress ratio, Fig.6 (c) however, remains largely unchanged. We note that time averages of the stresses at each phase angle have been taken due to the periodicity, which is the same as the applied vibration, as seen in the inset of Fig.6 (a) for the bulk normal stress (BNS).

To understand more quantitatively the stress profiles and effects of the vibration, we conduct a continuum analysis of the stresses as follows. Taking the granular bed volume fraction as constant, because of no significant bed dilation or compression, Fig. 6 (c), the momentum equations in x and z directions can be expressed respectively as:

$$\rho \phi \frac{dv_z}{dt} = -\frac{\partial \sigma_{zz}}{\partial z} - \rho \phi g \cos\theta, \tag{9}$$

$$\rho \phi \frac{dv_x}{dt} = -\frac{\partial \sigma_{xz}}{\partial z} + \rho \phi g \sin\theta, \tag{10}$$

where ρ is particle density. The normal stress gradient $-\partial\sigma_{zz}/\partial z$ (denoted as term A) should balance the total acceleration term ($\rho_s \Phi g \cos\theta + \rho \phi \frac{dv_z}{dt}$) ($B$), which was shown to be valid in Fig.7, indicated by the ratio of A/B close to unity calculated using the simulation data in Fig.6 (a). Because $\rho \phi \frac{dv_z}{dt}$, the bed acceleration, can be assumed to equal to the base acceleration, being 0 at T and 1/2T and -0.5g and 0.5g at 1/4T and 3/4T, respectively, it can be deduced from Eq. (10) that the normal stress gradients at T and 1/2T should be roughly the same as in the static case; and those at 1/4T and 3/4T should about 0.5 and 1.5 times of the static values respectively. These values are again consistent with the simulation observations in Fig.6 (a). The shear stress gradient should vary proportionally to the normal stress gradient since the stress ratio remains the same due to the microstructure similarity. As shown in Fig.7, the ratio between the shear stress gradient $\partial\sigma_{xz}/\partial z$ (C) and $\rho_s \Phi g \sin\theta$ (D) thus became about 0.5 and 1.5 at

1/4T and 3/4T, respectively. This imbalance leads to mobility, specifically acceleration (0-T/2) and deceleration (T/2-T), of the granular bed in the *x* direction, explaining the *x*-velocity variation within a cycle as observed in Fig. 4(a).

To quantitatively link the stress to the velocity profiles, an appropriate rheological model is needed. We show that the rheology is modified by vibration and cannot be described by the steady-state shear rheology, but leave developing new models for future work. The flow curves of steady-state shear rheology for granular flows as identified by Chialvo et al. [39] are used for the comparison. The master curves between the pressure $P^* = \frac{P}{\left|\phi - \phi_c\right|^{2/3}}$ and shear rate $\dot{\gamma}^* = \frac{\dot{\gamma}}{\left|\phi - \phi_c\right|^{4/3}}$ (solid lines in Fig.8) scaled by the distance to a critical volume fraction ϕ_c, describe the steady state granular flow behavior at all volume fractions and shear rates. They bridge the quasi-static, inertial and intermediate regimes [40], where the pressure is proportional to power 0, 2 and 1/2 of the shear rate, respectively. The data extracted from the simulation at different phase angles are plotted on this flow regime map and can be seen to fall in the region between the quasit-static and the inertial flow curves, Fig. 8, indicating a type of flow behaviour away from steady simple shear. Sections of negative slops can also be observed for these flow curves, suggesting flow instabilities.

In summary, the granular bed with inclination angel of 19° attains mobility because of the weakening of force network by vibration acceleration and presents overall solid-like flow, but with complex flow curves, suggesting an unsteady and instable behaviour. The above results call for closer attention to the surface-normal vibration in the field of geomechanics to complement the standard Newmark's method, which has been widely used to evaluate slope performance under seismic condition, but only considers the vibration along sliding surface [32-36].

4.3 Large deformation flow state

After the initial translational sliding state, landslides could transit to a large deformation flow state, which was modeled by chute flow with an inclination angle of 24° under the vibration of $0.1\sqrt{g/d}$ frequency. The chute flow at 24° without any vibration should

be inertial because it is above the angle of repose. Indeed, the x-velocity has a Bagnoldian profile for inertial flow [40], i.e., an upward parabola with velocity of zero at bottom, Fig. 9(a); the bulk volume fraction over the whole bed is about 0.57 and below the critical volume fraction Fig. 9(b). The pressure—shear rate data (red dashed line) collapse onto the inertial flow curve in Fig.8, also confirming its inertial behavoiur. The velocities at different phases under vibration present similar profiles, with the free surface velocity increased by up to 15%, Fig. 9(a). The enhanced mobility by vibration can lead to longer runout for landslides. In contrast to the 19° case, the granular bed experiences compression (1/2T—3/4T) and expansion within a cycle as shown by the time evolution of the bulk volume fraction in the inset of Fig. 9(b). This vibration-induced temporal Φ-variation implies mass flux in the z-direction – the granular bed thus behaves like a compressible fluid in this situation. The bulk volume fractions under vibration are lower than that without vibration except at the peak around 3/4T. The volume fractions are nearly constant along height, Fig. 9(b), except in the areas closed to bottom and the free surface and at the T/2 phase, when the volume fraction decreases along height. The spatial Φ-variation further indicate that even at each time instance the granular flow deviates from the steady inertial flow, which dictates a constant volume fraction in the height direction. The liquid-like characteristics are underpinned by a microstructure dominated by binary collisions, as demonstrated by the force networks in Fig. 10, in which the binary bonds are clearly visible especially for phases at 1/4T and 1/2T.

The complex transient dynamics are also reflected by the non-linear stress response as shown by the bulk normal stress evolution, which is periodic but not sinusoidal (inset of Fig.11 (a)). The profiles of normal stress, shear stress and the absolute value of stress ratio at different phase angles in Fig. 11 (a)—(c) respectively, are still largely linear, suggesting constant acceleration in x and z directions. The phase of the stress response is, however, out of synchronization with the vibration. This, together with the volume fraction and velocity deviations from the steady-state inertial flow profiles, suggests deviations in the rheology as well. The flow curves at different phase angles under

vibration, plotted in Fig.8, indeed deviate from the master curve although the stresses still largely exhibit the same 2nd power scaling with the shear rate. The granular material thus flows inertially, but with modified rheology. This calls for further research into the rheology of granular materials under vibration in order to better understand and predict the flow processes in earthquake-induced landslides.

5 Summary and conclusions

We have conducted DEM simulations on granular chute flows at 19° and 24° inclination angles subjected to surface-normal sinusoidal vibration with conditions relevant to earthquake-induced landslides. We found that lower frequency vibration has greater impact on the mobility at a fixed acceleration, 0.5*g*, typically observed in earthquakes. The effect of the vibration is, however, very different for the flows at 19° or 24° inclination.

The former flows like a solid with a connected force network, which maintains the anisotropy of stress transmission close to that for quasi-static flows. The internal stresses respond in phase to the vibration and are either decreased or increased depending on whether the vibration acceleration is acting in the same or opposite direction to the downward surface normal direction, respectively. The stress changes lead to imbalance in momentum and hence flow in the *x* direction. The rheological state deviates from either quasi-static or inertial steady flow and exhibits features of flow instability, probably setting the stage for the transition to large deformation flow. The latter flows inertially like a compressible fluid with flux in the *z* direction and having binary collisions dominating particle interactions. The stresses respond out of phase and are affected by vibration in a more complex way. The free surface velocity is increased by up to 15%.

6 Discussions and further remarks

The findings have a number of implications to the study of earthquake-induced landslides, the long runout of which remains a challenging problem to understand. First

of all, attention should be paid to the effect of vibration frequency in conjunction with acceleration magnitudes and to near-source pulse-like seismic waves of low frequencies for seismic analysis. The simulations revealed complex dynamics and rheology in the solid-like flow, which suggests that the sliding stage in a landslide could contain rich information for more accurate prediction of its dynamics and transition to large-deformation flow. The rheology for both cases is shown to deviate from the steady-state rheology, which warrants development of suitable constitutive models for such unsteady flows under vibration. Such efforts would ultimately contribute to understanding and predicting earthquake-induced landslides.

Finally, we note that the two cases studied in this paper can only reflect dynamical features at particular moments during a landslide. It is promising and interesting to use the discrete numerical approach to study the full landslide process including the transitions and considering more realistic soil properties and geological conditions in the future.

Acknowledgments

The authors acknowledge the support of the National Natural Science Foundation of China grants 51808401, 41728006 and 41831291, the China Postdoctoral Science Foundation grant 2017M620167 and the UK Natural Environment Research Council grant NE/R011001/1. We thank Dr. Thomas Barker for his useful discussions and careful editing of the final manuscript to improve the readability.

References

[1] Fan X, Juang CH, Wasowski J, et al. What we have learned from the 2008 Wenchuan Earthquake and its aftermath: A decade of research and challenges. Engineering geology 2018; 241: 25-32.

[2] Yin Y, Zheng W, Li X, et al. Catastrophic landslides associated with the M8. 0 Wenchuan earthquake. Bulletin of Engineering Geology and the Environment 2011; 70(1): 15-32.

[3] Xu C, Ma S, Tan Z, et al. Landslides triggered by the 2016 Mj 7.3 Kumamoto, Japan, earthquake. Landslides 2018; 15(3): 551-564.

[4] Stanley T, Kirschbaum DB. A heuristic approach to global landslide susceptibility mapping. Natural Hazards 2017; 87(1): 145-164.

[5] Shinoda M, Miyata Y, Kurokawa U, et al. Regional landslide susceptibility following the 2016 Kumamoto earthquake using back-calculated geomaterial strength parameters. Landslides 2019; 16(8): 1497-1516.

[6] Shrestha S, Kang TS. Assessment of seismically-induced landslide susceptibility after the 2015 Gorkha earthquake, Nepal. Bulletin of Engineering Geology and the Environment 2019; 78(3): 1829-1842.

[7] Muceku Y, Korini O, Kuriqi A. Geotechnical analysis of hill's slopes areas in heritage town of Berati, Albania. Periodica Polytechnica Civil Engineering 2016; 60(1): 61-73.

[8] Kuriqi A, Ardiçlioglu M, Muceku Y. Investigation of seepage effect on river dike's stability under steady state and transient conditions. Pollack Periodica 2016; 11(2): 87-104.

[9] Okada Y, Sassa K, Fukuoka H. Undrained shear behaviour of sands subjected to large shear displacement and estimation of excess pore-pressure generation from drained ring shear tests. Canadian Geotechnical Journal 2005; 42(3): 787-803.

[10] Collins GS, Melosh HJ. Acoustic fluidization and the extraordinary mobility of sturzstroms. Journal of Geophysical Research: Solid Earth 2003; 108(B10).

[11] Davies TR, McSaveney MJ. Runout of dry granular avalanches. Canadian Geotechnical Journal 1999; 36(2): 313-320.

[12] Wang YF, Xu Q, Cheng QG, et al. Spreading and deposit characteristics of a rapid dry granular avalanche across 3D topography: experimental study. Rock Mechanics and Rock Engineering 2016; 49(11): 4349-4370.

[13] Ugai K, Yang Q, Cai F, et al. Laboratory flume static and dynamic experiment for rock avalanches. Soil Dynamics and Earthquake Engineering 2010; 278-287.

[14] Yang Q, Ugai K, Cai F, et al. Small-Scale Flume Test under Dynamic Condition

for Rock Avalanches. The GeoHunan International Conference; 2011, p. 165-172.

[15] Chen G, Zen K, Zheng L, et al. A new model for long-distance movement of earthquake induced landslide. 44th US Rock Mechanics Symposium and 5th US-Canada Rock Mechanics Symposium; 2010.

[16] Zhang Y. 2018. Earthquake-Induced Landslides: Initiation and run-out analysis by considering vertical seismic loading, tension failure and the trampoline effect. Singapore: Springer Singapore; 2017.

[17] Zhang Y, Chen G, Zheng L, et al. Effects of near-fault seismic loadings on run-out of large-scale landslide: a case study. Engineering geology 2013; 166: 216-236.

[18] Zhang Y, Wang J, Xu Q, et al. DDA validation of the mobility of earthquake-induced landslides. Engineering Geology 2015; 194: 38-51.

[19] Huang CC, Lee YH, Liu HP, et al. Influence of surface-normal ground acceleration on the initiation of the Jih-Feng-Erh-Shan landslide during the 1999 Chi-Chi, Taiwan, earthquake. Bulletin of the Seismological Society of America 2001; 91(5): 953-958.

[20] Wu JH, Lin JS, Chen CS. Dynamic discrete analysis of an earthquake-induced large-scale landslide. International Journal of Rock Mechanics and Mining Sciences 2009; 46(2): 397-407.

[21] Gaudel N, De Richter SK. Effect of vibrations on granular material flows down an inclined plane using DEM simulations. Powder technology 2019; 346: 256-264.

[22] Cundall PA, Strack ODL. A discrete numerical model for granular assemblies. Géotechnique 1979; 29(1): 47-65.

[23] Silbert LE, Ertaş D, Grest GS, et al. Granular flow down an inclined plane: Bagnold scaling and rheology. Physical Review E 2001; 64(5): 051302.

[24] Silbert LE, Landry JW, Grest GS. Granular flow down a rough inclined plane: transition between thin and thick piles. Physics of Fluids 2003; 15(1): 1-10.

[25] Plimpton S. Fast parallel algorithms for short-range molecular dynamics. Journal of computational physics 1995; 117(1): 1-19.

[26] Liu S, Wang J, Kwok CY. DEM simulation of creep in one-dimensional

compression of crushable sand. Journal of Geotechnical and Geoenvironmental Engineering 2019; 145(10): 04019060.

[27] Perez JCL, Kwok CY, O'Sullivan C, et al. Exploring the micro-mechanics of triaxial instability in granular materials. Géotechnique 2016; 66(9): 725-740.

[28] Otsubo M, O'Sullivan C, Shire T. Empirical assessment of the critical time increment in explicit particulate discrete element method simulations. Computers and Geotechnics 2017; 86: 67-79.

[29] Perez JCL, Kwok CY, Senetakis K. Effect of rubber size on the behaviour of sand-rubber mixtures: a numerical investigation. Computers and Geotechnics 2016; 80: 199-214.

[30] Huang MH, Fielding EJ, Liang C, et al. Coseismic deformation and triggered landslides of the 2016 Mw 6.2 Amatrice earthquake in Italy. Geophysical Research Letters 2017; 44(3): 1266-1274.

[31] Sun J, Battaglia F, Subramaniam S. Dynamics and structures of segregation in a dense, vibrating granular bed. Physical Review E 2006; 74(6): 061307.

[32] Newmark NM. Effects of earthquakes on dams and embankments. Géotechnique 1965; 15(2): 139-160.

[33] Khalaj S, BahooToroody F, Abaei MM, et al. A methodology for uncertainty analysis of landslides triggered by an earthquake. Computers and Geotechnics 2020; 117: 103262.

[34] Pathak SR, Munnoli SS. Dynamic Active Earth Pressure on Flexible Cantilever Retaining Wall. International Journal of Geological and Environmental Engineering 2016; 9(7): 891-895.

[35] Saygili G, Rathje EM. Empirical predictive models for earthquake-induced sliding displacements of slopes. Journal of Geotechnical and Geoenvironmental Engineering 2008; 134(6): 790-803.

[36] Hsieh SY, Lee CT. Empirical estimation of the Newmark displacement from the Arias intensity and critical acceleration. Engineering Geology 2011; 122(1-2): 34-42.

[37] Butler R. High-Frequency (> 100 Hz) Earthquakes North of Moloka'i Detected on the Seafloor at the Aloha Cabled Observatory. Bulletin of the Seismological Society of America 2018; 108(5A): 2739-2747.

[38] Azéma E, Radjai F. Internal structure of inertial granular flows. Physical review letters 2014; 112(7): 078001.

[39] Chialvo S, Sun J, Sundaresan S. Bridging the rheology of granular flows in three regimes. Physical review E 2012; 85(2): 021305.

[40] MiDi GDR. On dense granular flows. The European Physical Journal E 2004; 14(4): 341-365.

List of Figure Captions

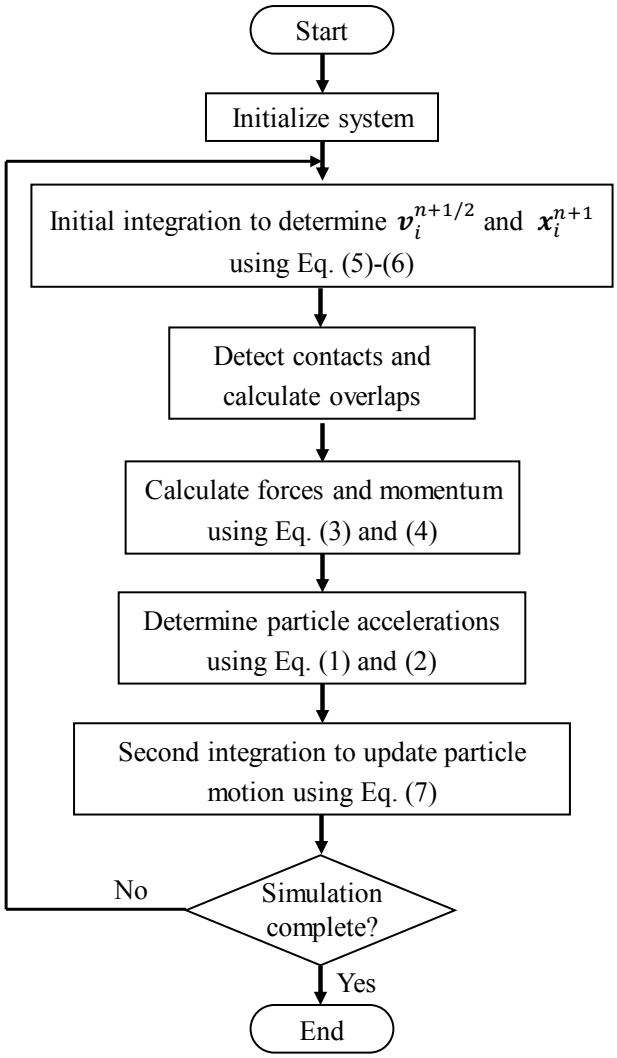

Fig. 1 Flowchart of the DEM algorithm

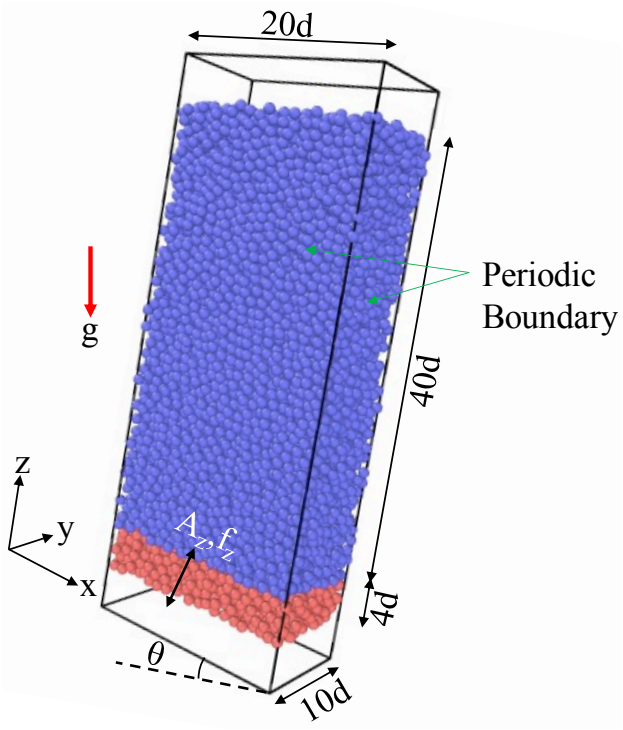

Fig.2 Configuration of the chute flow model

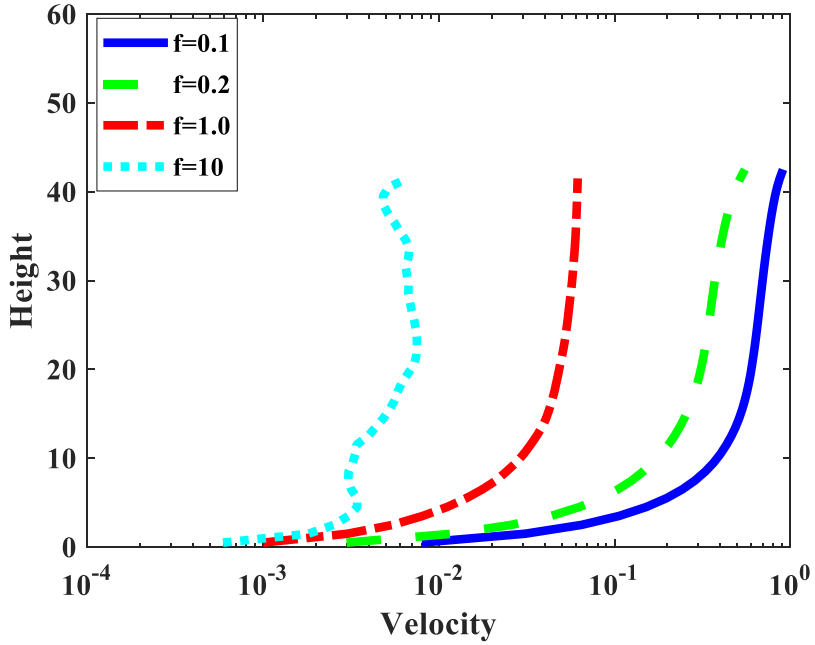

(a) θ=19°

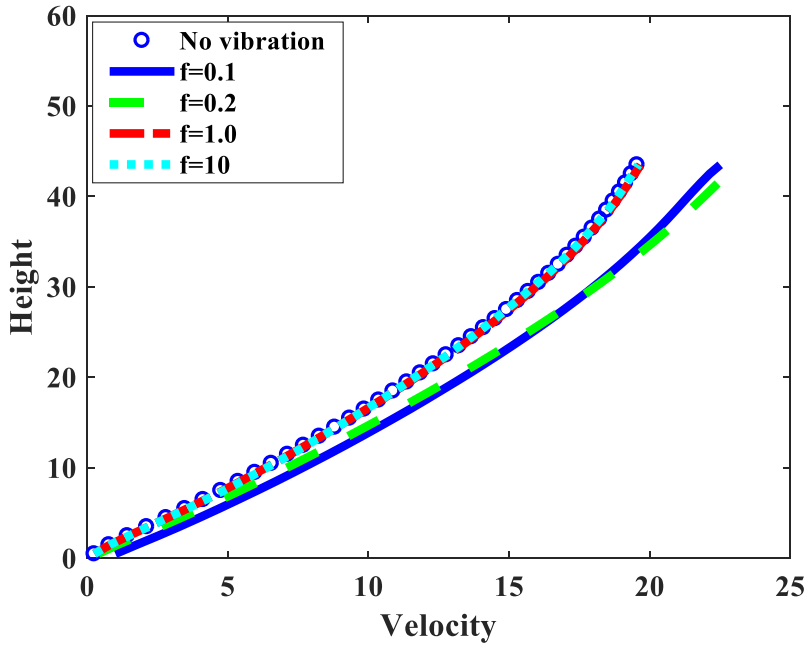

(b) θ=24°

Fig. 3 x-direction velocity profiles at 1/2T under z-direction vibration with different frequency: (a) θ=19°. (b) θ=24°.

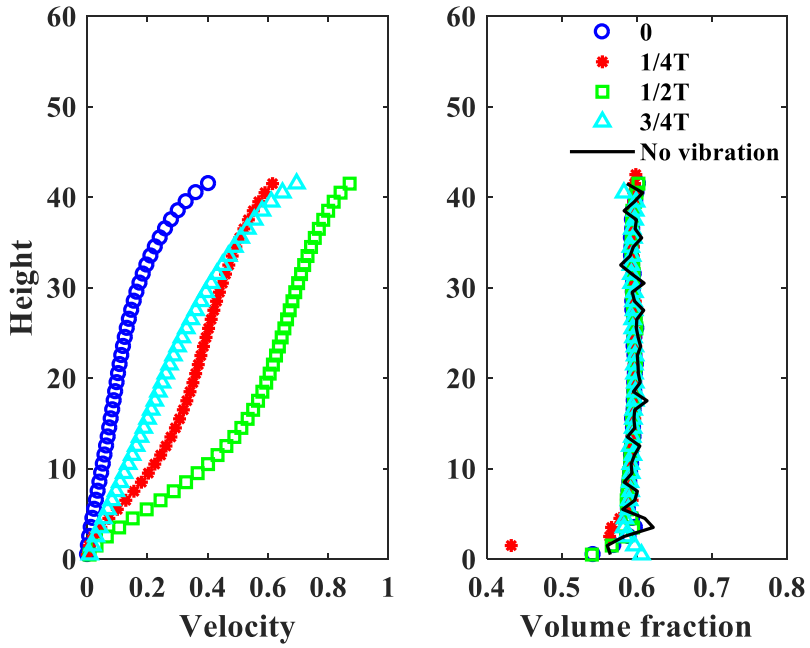

(a) (b)

Fig.4 Velocity and volume fraction profiles at different phases angle for θ=19°: (a) x-velocity profiles. (b) volume fraction profiles.

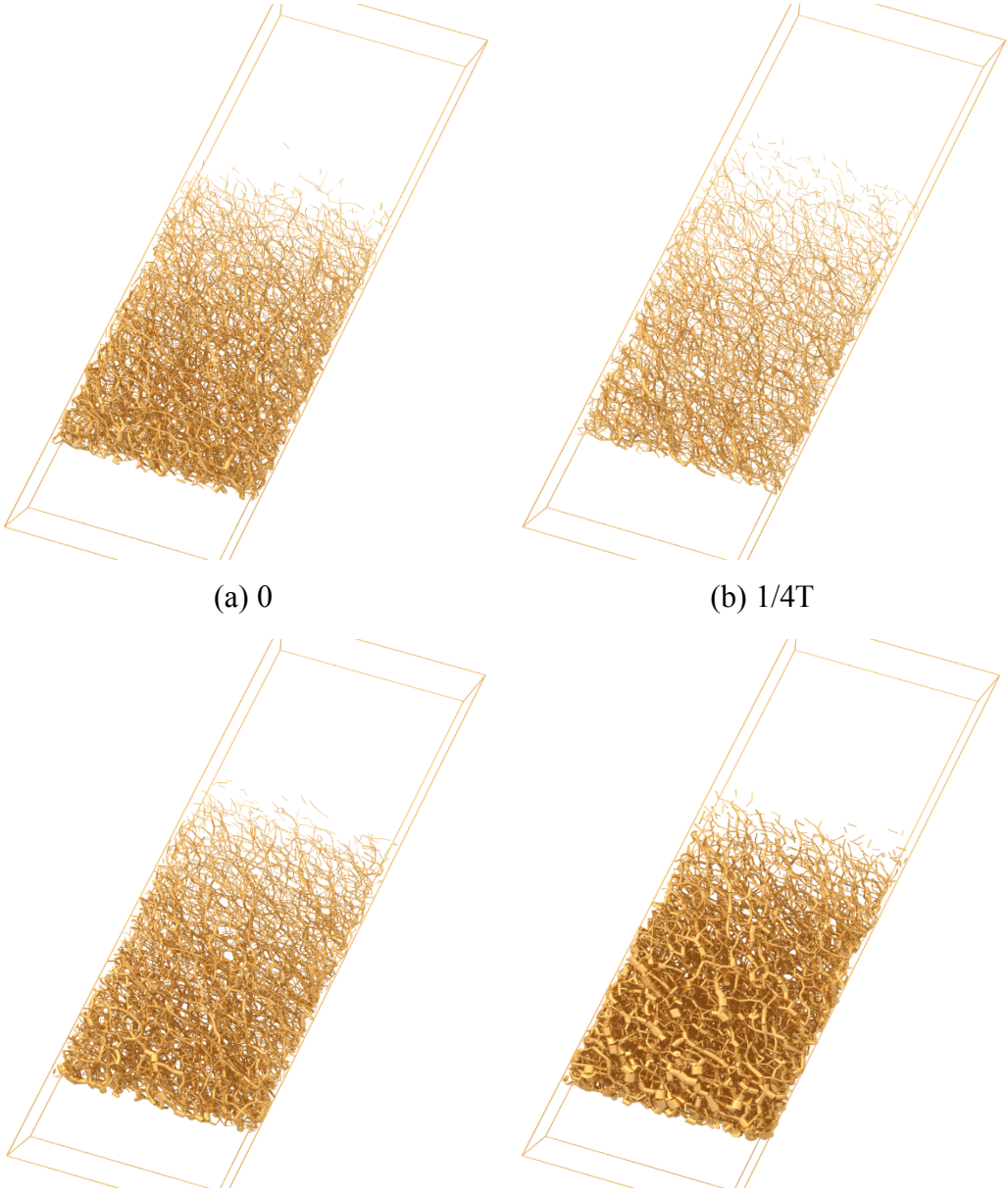

(a) 0 (b) 1/4T

(c) 1/2T (d) 3/4T

Fig.5 Force networks in the granular system at different phase angles for θ=19°: (a) 0. (b) 1/4T. (c) 1/2T. (d) 3/4T.

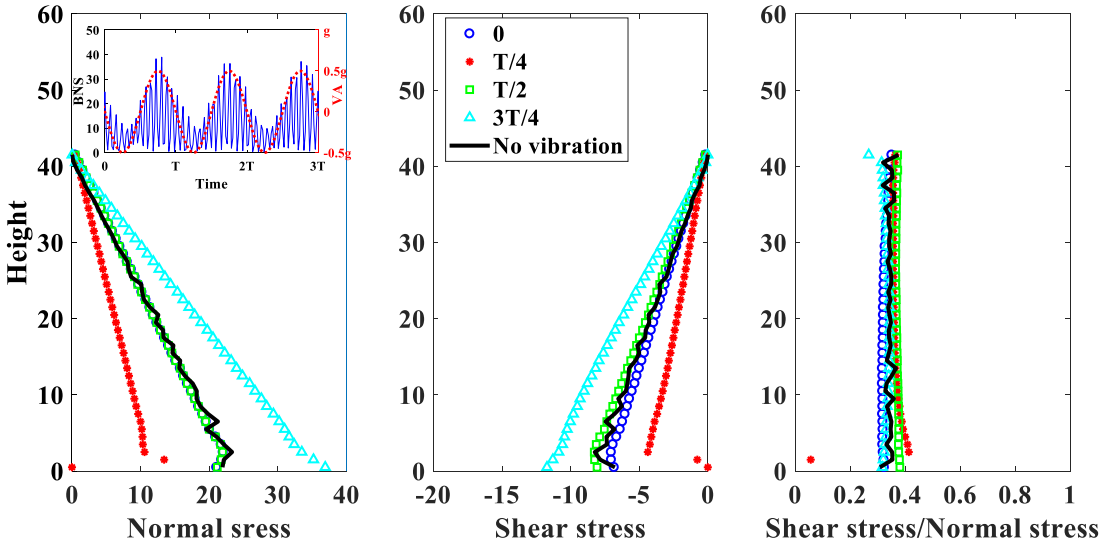

(a) (b) (c)

Fig.6 Stress profiles and stress ratio at different phases angle for θ=19°: (a) normal stress profiles; Inset: Time history of bulk normal stress (BNS) and vibration acceleration (VA). (b) shear stress profiles. (c) Absolute value of stress ratio.

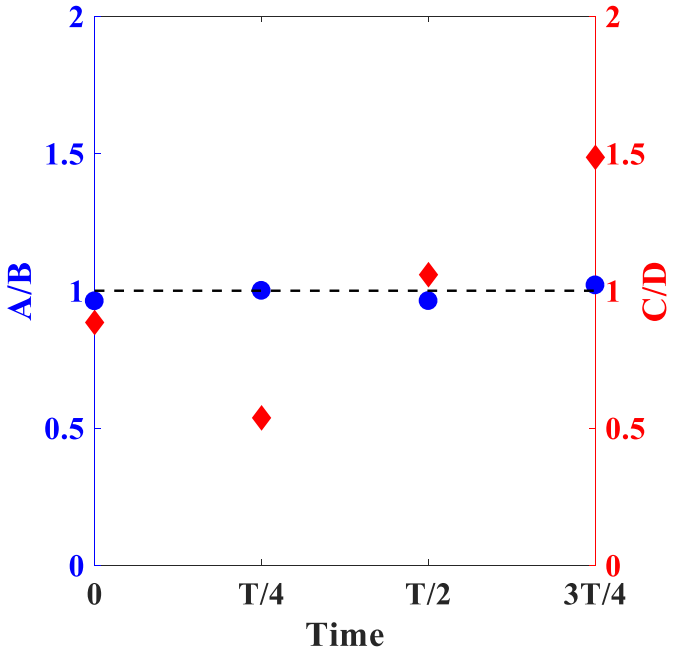

Fig.7 The relationship between different terms of momentum equations for θ=19° (Z: A=$-\partial\sigma_{zz}/\partial z$, B=$\rho_s \Phi g \cos\theta + \rho\phi\frac{dv_z}{dt}$; X: C=$\partial\sigma_{xz}/\partial z$, D=$\rho_s \Phi g \sin\theta$).

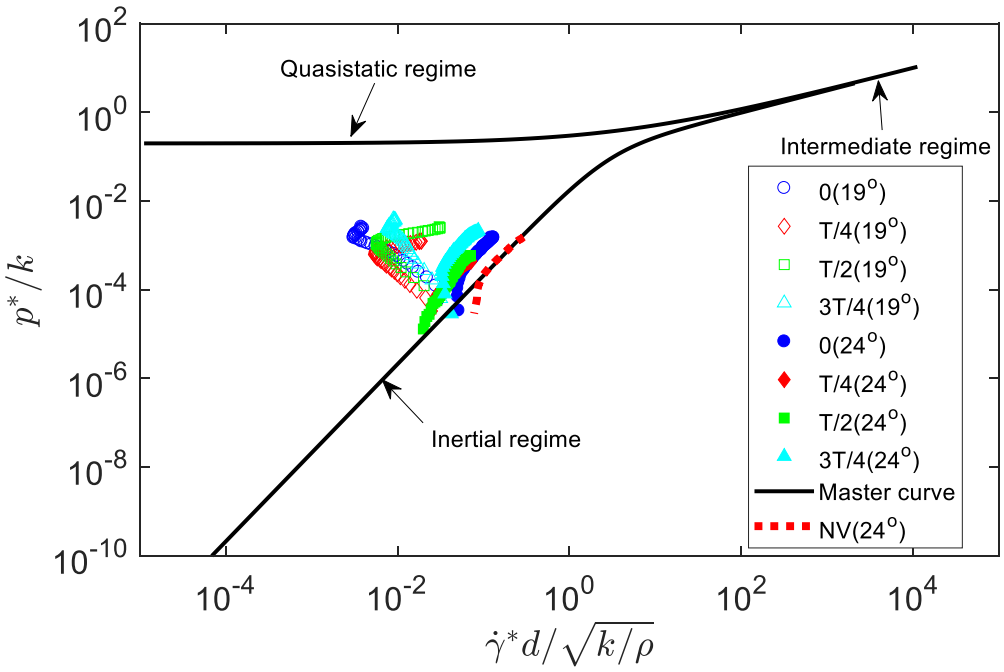

Fig.8 Relationship between dimensionless pressure and dimensionless shear rate at different phase angle (NV is abbreviation of no vibration). The curves describe the steady-state rheological model proposed by Chialvo et al. (2012).

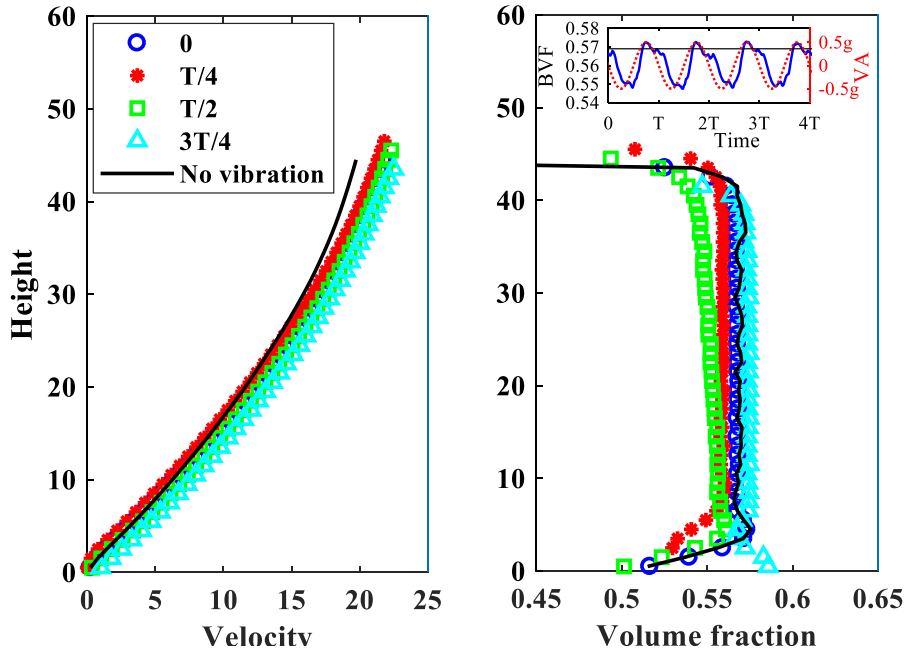

(a) (b)

Fig.9 Velocity and volume fraction profiles at different phases angle for θ=24°: (a) *x*-velocity profiles. (b) volume fraction profiles; Inset: Time history of bulk volume fraction (BVF) and vibration acceleration (VA).

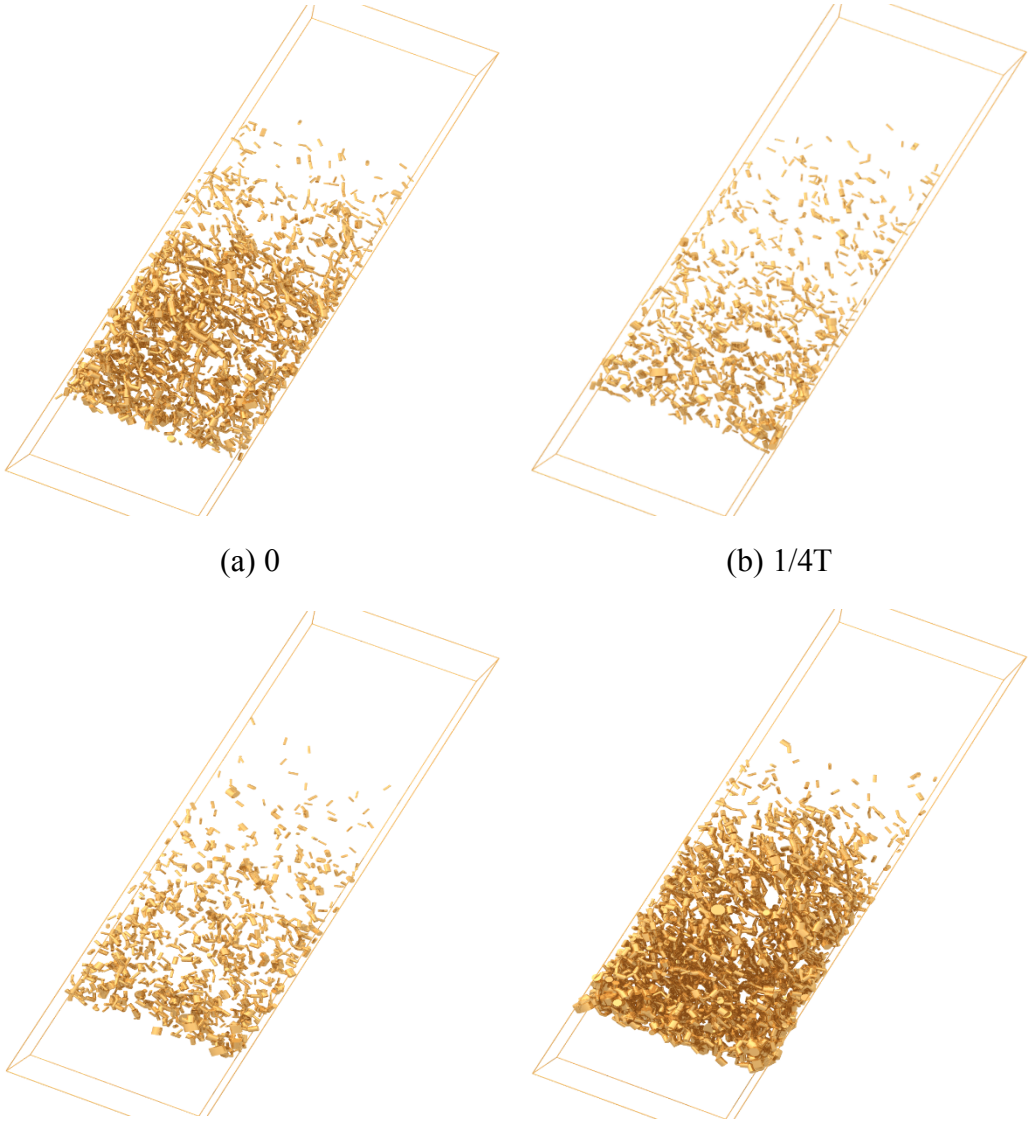

(a) 0 (b) 1/4T

(c) 1/2T (d) 3/4T

Fig. 10 Force networks in the granular systems at different phase angles for θ=24°: (a) 0. (b) 1/4T. (c) 1/2T. (d) 3/4T.

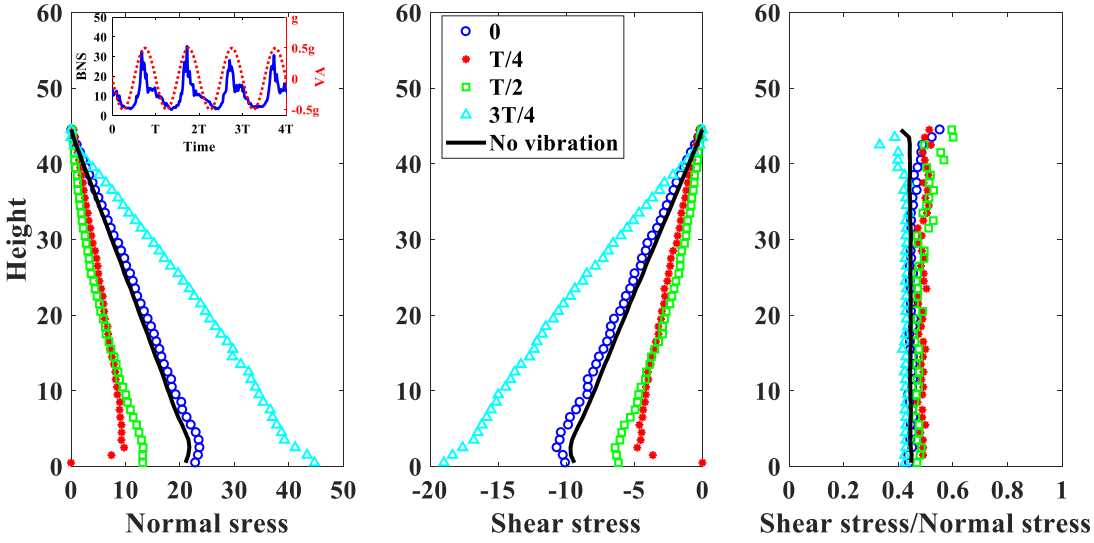

(a) (b) (c)

Fig.11 Stress profiles and stress ratio at different phases angle for θ=24°: (a) normal stress profiles; Inset: Time history of bulk normal force (BNS) and vibration acceleration (VA). (b) shear stress profiles. (c) Absolute value of stress ratio.